Experimental and computational investigations of a normal-hole bled supersonic boundary-layer

J. M. Oorebeek[*], and H. Babinsky[†]

Cambridge University, Cambridge, CB2 1PZ, United Kingdom

M. Ugolotti[‡], P. Orkwis[§], and S. Duncan[¶]

University of Cincinnati, Cincinnati, Ohio, 45221, USA

A series of experiments have been conducted on a bleed hole array spanning the width of the CUED supersonic wind tunnel at Mach numbers of 1.8 and 2.5. The wind tunnel was run with varying levels of suction, and the flow structure over the bleed array was subsequently mapped with a Laser Doppler Velocimetry (LDV) system at a resolution of 0.25 hole diameters or better. The same wind tunnel setup was simulated using the **OVERFLOW** Navier-Stokes equation solver. The information obtained was used primarily in qualitative comparisons of flow patterns. Overall good agreement was found in the definition of the expansion fan and barrier shock pattern produced by flow entering the normal holes, as well as 3D flow patterns. Both studies agreed well in terms of measured mass flow rates, to within 1% of the boundary layer mass flow. The presence of the barrier shock standing off the downstream edge of the bleed holes corresponded with a jet of upwards flow, which may provide a mechanism for the generation of streamwise vorticies.

I.   Nomenclature

Roman symbols

A — Area (m^2)

---

[*]Research Student, Department of Engineering. Now at Pratt & Miller Engineering. Student Member AIAA

[†]Professor, Department of Engineering. Associate Fellow AIAA.

[‡]Visiting Scholar, Department of Aerospace Engineering and Engineering Mechanics, ML 70. Student Member AIAA

[§]Bradley Jones Professor and Head, Department of Aerospace Engineering and Engineering Mechanics, ML 70. Associate Fellow AIAA

[¶]Graduate Research Assistant, Department of Aerospace Engineering and Engineering Mechanics, ML 70. Student Member AIAA

American Institute of Aeronautics and Astronautics

d	Bleed hole, or orifice, diameter (mm)
H	Boundary layer shape factor $\left(\equiv \frac{\delta^*}{\theta}\right)$
h	Working section height (mm)
M	Mach number
$\dot{m}$	Mass flow rate (kg/s)
$\dot{m}_{\text{sonic}}$	Sonic mass flow rate $= A\sqrt{\frac{\gamma}{R}}\frac{P_o}{\sqrt{T_o}}\left(\frac{2}{\gamma+1}\right)^{\frac{1}{2}\left(\frac{\gamma+1}{\gamma-1}\right)}$
$\dot{m}_{bl}$	Boundary layer mass flow rate $= w\rho_e U_e(\delta - \delta_c^*)$
P	Pressure (Pa)
P_r	Pressure ratio P_{pl}/P_e
Q_{sonic}	Sonic flow coefficient $\dot{m}/\dot{m}_{\text{sonic}}$
R	Ideal gas constant for air $= 287\ Jkg^{-1}K^{-1}$
Re_{θ_c}	Reynolds number based on compressible momentum thickness $(\equiv U_e\theta_c/\nu)$
T	Temperature (K)
U, V, W	Local velocity (streamwise, wall normal, spanwise) (m/s)
w	Working section width (mm)
x, y, z	Local coordinates (streamwise, wall normal, spanwise) (mm)
y^+	Non-dimensional distance $\left(\equiv \frac{yu_\tau}{\nu_w}\right)$

Greek letters

γ	Ratio of specific heats $\left(\equiv \frac{c_p}{c_v}\right) = 1.4$ for air
δ	Boundary layer thickness (mm), where $U(\delta) = 0.995U_\infty$
δ_c^*	Compressible displacement thickness (mm) $\left(\equiv \int_0^\infty \left(1 - \frac{u\rho}{U_e\rho_e}\right)dy\right)$
δ_i^*	Incompressible displacement thickness (mm) $\left(\equiv \int_0^\infty \left(1 - \frac{u}{U_e}\right)dy\right)$
θ_c	Compressible momentum thickness (mm) $\left(\equiv \int_0^\infty \frac{u\rho}{U_e\rho_e}\left(1 - \frac{u\rho}{U_e\rho_e}\right)dy\right)$
θ_i	Incompressible momentum thickness (mm) $\left(\equiv \int_0^\infty \frac{u}{U_e}\left(1 - \frac{u}{U_e}\right)dy\right)$
μ	Dynamic viscosity $(kg/(ms))$
ν	Kinematic viscosity $\left(\equiv \frac{\mu}{\rho}\right)(m^2/s)$
ρ	Density (kg/m^3)
τ	Shear stress (Pa)

American Institute of Aeronautics and Astronautics

Subscripts

b	Baseline conditions
c	Compressible flow conditions
e	Boundary layer edge conditions
i	Incompressible conditions
o	Stagnation condition
pl	Plenum conditions

II. Introduction

A. Overview

Shock-Wave/Boundary Layer Interactions (SWBLIs) are unavoidable consequences of high speed flight, observed when normal or oblique shocks interact with a boundary layer on a surface, potentially causing the flow to separate.[1] While found in many areas of modern aerodynamics, their greatest impact can be felt in supersonic inlets. Here, the inlet must provide the engine with low loss, uniform subsonic flow. As shock losses increase with the shock strength, at high Mach numbers multiple oblique shocks are generally employed to gradually slow the flow. While these multi-shock systems are good at preserving total pressure, the longer inlet creates a thicker boundary layer more susceptible to shock induced separation. Inlets can be designed to have all necessary shocks occur outside the main inlet duct, in a manner known as external compression, or the shocks can be held internal to the duct, giving either mixed or fully internal compression inlets.[2] In such a system bleed must be used through the entire inlet to both limit boundary layer growth and prevent flow separation around these SWBLIs.

Although bleed provides numerous benefits to the inlet system, its use comes at a cost of increased drag and weight of the aircraft. Inlets must be made larger to accomodate the removal of anywhere between 3 and 15% of the total inflow,[3] while the vented bleed air increases the momentum deficit of the aircraft wake. Consequently, there is a movement to design engine inlets with a reduced need for bleed. To accomplish this, a greater understanding of how suction affects the flow must be attained, through a combined effort of experimental and numerical investigations.

B. Previous Work

Effective numerical modelling of bleed has been in use for a number of years, as discussed in the review paper by Hamed and Shang.[4] A summary of roughness and turbulence model adjustments to account for bleed can be found in Paynter, et al.[5] who further developed the roughness modeling approach in a distributed bleed

American Institute of Aeronautics and Astronautics

patch. This was followed by the works of Slater and Saunders[6] and Slater[7] who developed and extended (respectively) a velocity boundary condition to incorporate bleed effects.

In a similar timeframe researchers like Benson, et al.,[8] Chyu, et al.[9] and Shih, et al.[10] were simulating bleed hole flow and investigating the structure of supersonic bleed. Subsequently Li et. al.,[11] Hamed et al.[12] and Orkwis et. al.,[13] explored both simulations and models based on the Slater approach. These efforts have found that surface boundary conditions alone have great difficulty providing accurate bleed predictions that include both mass removal and the subsequent downstream flow effect.

While these models have progressed in terms of fidelity and scale, the necessary data to validate these models has been sorely lacking. Information has primarily been restricted to flow coefficients and boundary layer velocity profiles both with and without an impinging oblique shock wave,[14–17] with only a few glimpses of the more complex 3D flow structure surrounding individual bleed holes[18, 19] and their interaction within an array. Jointly, these experiments and models have helped to establish an idea of the canonical flow through supersonic bleed holes. Flow is initially turned towards the hole through expansion fans, and then subjected to a barrier shock as it turns around the downstream edge of the hole. These waves also appear to propagate readily in all three dimensions. The creation of streamwise vorticity has also been readily shown in subsonic experiments of bleed holes,[20] but not reliably shown in the supersonic case.

C.   Current Research

In order to better develop models of bleed for flow control in inlets, this paper continues the experimental study started at the University of Cambridge,[21] combining it with high resolution CFD from the University of Cincinnati.[13] Experiments and computations were run with Mach 1.8 and 2.5 flow over a bleed region comprising of 2mm diameter normal holes, a setup applicable to performance bleed in mixed compression inlets. The goal is to better develop the CFD modeling tools, and validate the computational results with experimental data. Additionally, more information about the 3D flow structure around the bleed holes is desired, to better anticipate additional effects of bleed arrays.

III.   Investigation Methods

A.   Wind Tunnel Experiments

A set of experiments were devised to characterize the effects of bleed on the boundary-layer in supersonic flows. A blow-down type supersonic wind tunnel at the University of Cambridge, shown in figure 1, was used to conduct experiments at Mach numbers of 1.8 and 2.5. The baseline characteristics for each Mach number are shown in table 1. The working section has a cross section of 114mm wide by 85mm high in its half-liner configuration, with a region approximately 200mm long for the mounting of experiments and optical access.

American Institute of Aeronautics and Astronautics

Streamwise measurement locations will be given relative to the center of the last row of bleed holes, with x = 0 near the approximate center of the working section window.
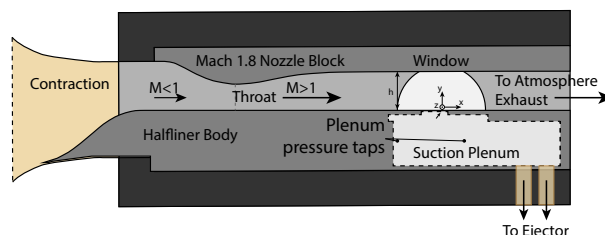

Figure 1. Schematic of wind tunnel arrangement for Mach 1.8 setup.

Table 1. Baseline, undisturbed turbulent boundary layer conditions from $x = -34$ mm.

		Mach 1.8	Mach 2.5
U_e	[m/s]	475	578
δ	[mm]	5.8	6.2
$\delta_i^*(\delta_c^*)$	[mm]	0.763 (1.26)	0.873 (1.84)
$\theta_i(\theta_c)$	[mm]	0.584 (0.492)	0.648 (0.463)
$H_i(H_c)$		1.30 (2.65)	1.34 (3.86)
$Re_{\theta_c} \cdot 10^{-3}$		16.2	13.9
$\dot{m}_{BL}$	[kg/s]	0.211	0.137
P_e/P_o		0.171	0.0584
P_o	[kPa]	239.5	308.4

Velocity measurements were obtained using a two-component Laser Doppler Velocimetry (LDV) system. A Coherent Innova 5W continuous Argon-Ion laser led into a TSI optics system, allowing for two components of velocity (streamwise and wall-normal) to be resolved. Seeding was provided by kerosene droplets approximately 200–500nm in diameter, with a maximum Stokes number of 0.115, providing confidence that the particles are small enough to follow the flow with little lag.[22] A motorized traverse allowed multiple measurements in all three directions (streamwise, spanwise and wall-normal) to be taken during a single wind-tunnel run. The typical spacing between measurement points was 0.1–0.5 mm, with the capability of measuring down to 0.1mm from the wall, corresponding to y^+ $\mathcal{O}(100)$. Boundary layer traverse data from the LDV system was used to generate the boundary layer integral parameters in table 1.

The LDV measurement volume can generally be aligned to an absolute position inside the wind tunnel to within $\pm 0.2mm$ in the streamwise direction, ± 0.1mm in the spanwise direction, and ± 0.02mm in the wall normal direction. The relative spacing between measurements, however, is accurate to within 0.02mm or better. While the measurement volume is quite small in the streamwise and wall-normal directions (of the order of 0.1mm), the fringes of the measurement volume extend 0.5mm further to either side. While these fringes are lower intensity than near the center of the measurement volume, this can still cause some

American Institute of Aeronautics and Astronautics

uncertainty in the measured velocity.

Measurement uncertainty of the LDV system is predicted by thorough analysis in Nolan[23] and Colliss,[24] summarized here. Due to geometric resolution of the two measured components of velocity, the streamwise velocity signal (U) has a certainty ranging from 2m/s in the freestream, to 5m/s at the closest point to the wall (0.2mm). The wall-normal velocity measurement is subjected to greater uncertainty, from 3m/s in the freestream, to 6m/s at the closest point to the wall.

All pressures were measured with a Pressure Systems[TM] Netscanner, capable of reading ±15psig within the working section, and ±45psig for the settling chamber pressure. Pressure taps with an internal diameter of 0.3mm were used to measure static pressure to within ±1.5%, while the stagnation pressure measured within the settling chamber was known to within ±1%.

B.   Flow Visualization

A Schlieren system was used to visualize density variations within the flow. Each mirror had a diameter of 208mm, and focal length of 2.4384m (8ft). A 'Z' arrangement of mirrors was used, as described in Oorebeek.[22] A horizontal cutoff was used to highlight density gradients through the boundary layer. A Nikon D7000 camera was used to capture the resulting schlieren images, with an exposure time of 1/400s.

C.   Suction System

The suction system was powered by an ejector driven from the same high-pressure air supply used for the wind tunnel. A vacuum pressure of approximately 5kPa could be generated, entraining up to 0.050kg/s. This corresponds to approximately 20% of the incoming floor boundary layer mass flow, or 1.5% of the total tunnel mass flow. The ejector was connected to the bleed plenum via an interchangeable orifice plate instrumented with corner pressure taps. This arrangement served to both control and measure the suction mass flow. The suction mass flow rate was determined by the pressure ratio across the orifice, using the methods outlined in Ref. 25 and Ref. 26. The uncertainty in the mass flow measured by the orifice plate is 2%. All joints within the suction system were sealed with a gasket sealant, restricting the leak rate to approximately 0.0035kg/s. Leak rates were estimated by reducing the orifice diameter until the plenum pressure exceeded the working section pressure, while mass flow was still registered at the orifice plate - this mass flow rate was considered to be flow which did not pass through the bleed plate itself, but through gaps in the system. The corrected mass flow rate is what is shown in this paper.

The suction plenum was instrumented with 2 wall-mounted static pressure taps shown in figure 1, out of the influence of any jets issuing from the bleed holes. The suction plenum was 380mm long, 94mm wide and 125mm deep. Suction was applied to the wall of the wind tunnel via an interchangeable plate with 193
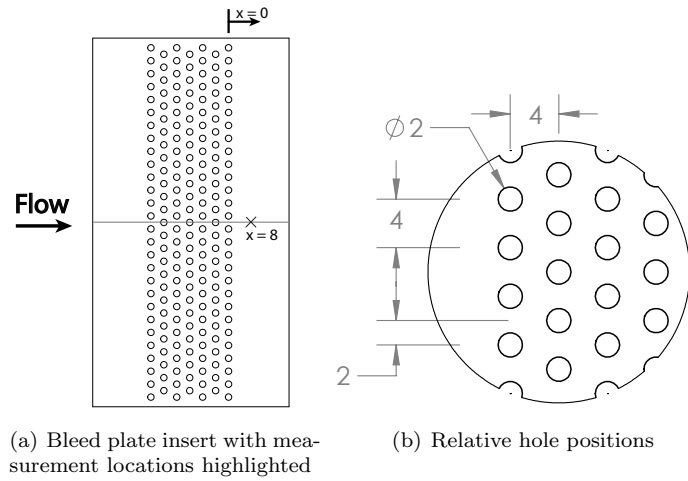
American Institute of Aeronautics and Astronautics

(a) Bleed plate insert with measurement locations highlighted

(b) Relative hole positions

Figure 2. Bleed plate insert and geometry, with measurement station indicated by cross. All dimensions in mm

discrete 2mm diameter circular holes, normal to the wall, shown in figure 2. The ratio of hole diameter to local compressible displacement thickness d/δ_c^* ranged from 1.6 at Mach 1.8 to 1.1 at Mach 2.5. The holes were drilled through a 3mm thick plate, thus the ratio of hole length to diameter was 1.5.

The sonic flow coefficient Q_{sonic} is used to quantify the efficiency of a suction device by comparing the flow rate through the holes to an ideal case, where the flow is choked through the holes with no separation, shown in equation 1.[27] This parameter is particularly important in the Slater model of bleed holes, which provides a model of bleed hole behaviour without any explicit dependence on the freestream Mach number.[7]

$$Q_{sonic} = \frac{\dot{m}}{\dot{m}_{sonic}}, \text{where } \dot{m}_{sonic} = A\sqrt{\frac{\gamma}{R}}\frac{P_o}{\sqrt{T_o}}\left(\frac{2}{\gamma+1}\right)^{\frac{1}{2}\left(\frac{\gamma+1}{\gamma-1}\right)}. \tag{1}$$

The suction strengths for the various experimental conditions are outlined below, in table 2. Data from the previous experiments of Oorebeek and Babinsky[21] are re-presented, as well as more recent experimental data. The ratio between the plenum pressure and freestream pressure $\frac{P_{pl}}{P_e}$ is shown as P_r to identify each case presented.

D.   Simulation and Modeling Techniques

1.   Flow Solver and Boundary Conditions

OVERFLOW employs the three-dimensional, steady (or unsteady) Reynolds Averaged Navier Stokes (RANS) equations and permits the use of multigrid and grid-sequencing to reduce convergence time. The code employs an overset gridding methodology that allows intricate and complicated geometry to be easily resolved. This method works by overlapping the many blocks required to model geometry, thus increasing flexibility in the development of the mesh and permitting rapid solution change. For these simulations, the HLLC flux

American Institute of Aeronautics and Astronautics

Table 2. Suction strength quantities for all cases. First two datasets from Oorebeek and Babinsky.[21] Final dataset is new data.

Mach	$\frac{P_{pl}}{P_o}$	P_r	$\dot{m}$ (g/s)	Q_{sonic}	$\%BL$
1.8	0.147	0.888	6	0.0175	3.3
From [21]	0.055	0.327	24	0.0728	13.8
2.5	0.053	0.914	2	0.0042	1.4
From [21]	0.025	0.433	11	0.0246	8.3
1.8 (new)	0.143	0.811	6	0.0175	2.9
	0.090	0.513	19	0.0612	9.7
	0.051	0.296	24	0.0692	12.1
1.8 (CFD)	0.143	0.880	5.7	0.0166	2.6
	0.053	0.304	19.2	0.0618	8.8
2.5 (CFD)	0.025	0.433	12.5	0.0230	9.2
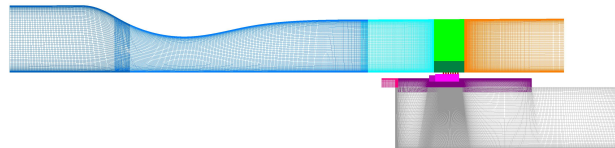
Figure 3. Mesh for Mach 1.8 arrangement.

scheme, SST Turbulence model, Koren flux limiter, and a 3rd-order spatial discretization were used. Previous simulations of similar cases[13] had utilized the SST Turbulence model to provide convergent analysis and reliable results, thus was retained for this work.

2. *Grid and Geometry*

The CFD model analyzes a center slice of the wind tunnel and includes the nozzle block (thus, excludes the settling chamber and contraction), the bleed holes and the plenum; the dimensions of these components are reproduced directly from the experimental apparatus. This approach provides for a finer grid without requiring an excessive computational burden. The slice is 4mm wide in the spanwise direction, encompassing two half-holes or one full-hole from each row of the pattern. Figure 3 shows the grid geometry for the Mach 1.8 tunnel, and the mesh created to discretize the fluid domain. The distribution of the bleed holes and the grid used for the holes, the first portion of the test section, and for the top of the plenum, are shown in figure 4.

The whole grid is made of 8.5 million and 8.3 million cells for Mach 1.8 and Mach 2.5 cases, respectively. The mesh inside the holes counts around half million cells and 2.8 million cells are used to model the plenum. Figure 4 shows the basic connection of the main tunnel flow field to the plenum through the bleed holes, thus employing the overlap technique. Values of y^+ for the first cell from the wall are of order 1. Mesh resolution

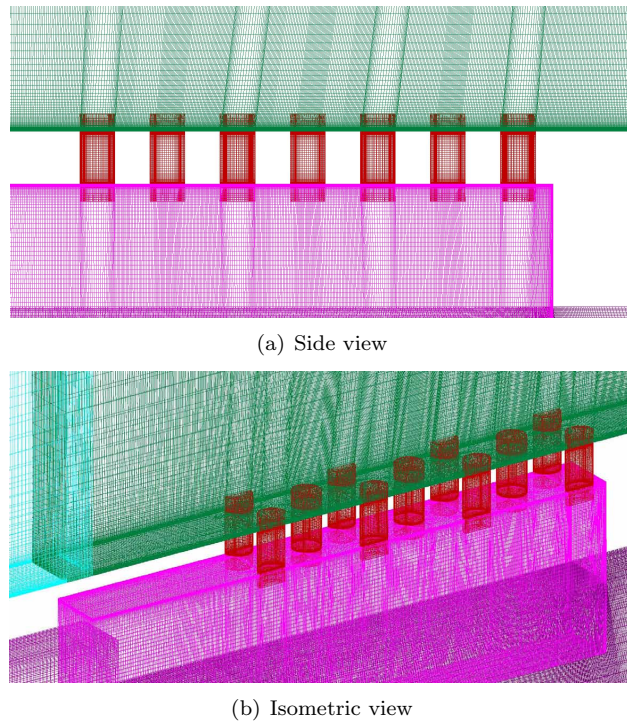(a) Side view

(b) Isometric view

Figure 4. Detail view of the mesh in the vicinity of the bleed hole array.

was enhanced in the boundary layer to capture detailed hole effects, but was not similarly improved in the main flow. This can lead to under-resolved flow-features in the freestream.

3. Boundary Conditions

No-slip, adiabatic walls are applied for all solid surfaces in the entire model. Starting from experimental parameters, the stagnation pressure and stagnation temperature are imposed on the inflow section of the tunnel while the outflow surface is set using a characteristic boundary condition approach, i.e. defining the static pressure equal to the freestream static pressure. The suction mass flow rate is reproduced from the experiments by imposing a specific pressure boundary condition on the two exit sections located in bottom surface of the plenum and the suction strength can be modified by changing the pressure difference between tunnel and plenum. Since the computational model is a slice of the actual geometry, a symmetric boundary condition is applied on the sidewalls of the tunnel, plenum and on the cutting planes of the half-holes. The influence of viscous effects generated by the sidewalls of the wind tunnel were considered negligible, as the data was gathered along the centerline of the tunnel, far away from bounding solid surfaces, and no shock wave was present.
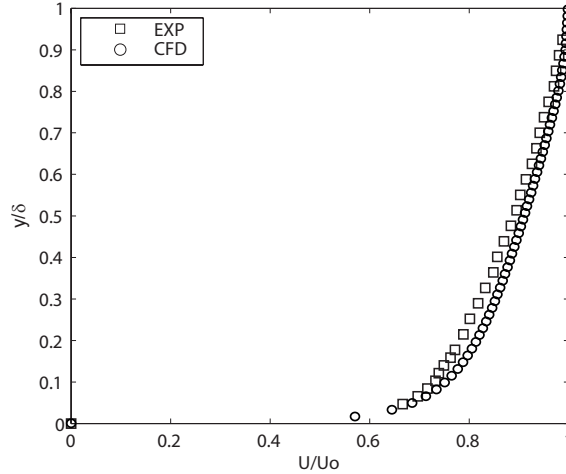
American Institute of Aeronautics and Astronautics

Figure 5. Comparison of Mach 1.8 inflow boundary layer for CFD and Experiments, $x = -34$

E.   Comparison between CFD and Experiments

Although the main thrust of this work is to provide a qualitative comparison between experimental and CFD results, it is prudent to look at how closely the CFD case matches with the experiment. Comparison of the Mach 1.8 inflow boundary layer is shown in figure 5, showing CFD boundary layer profile to be slightly fuller than the experimental. The differences between CFD and experimental data are presented in table 3. The similarity of the key properties gives confidence in making qualitative comparisons between experiments and CFD, however the subtle differences between the two flow fields would introduce additional uncertainty in detailed quantitative comparisons. In particular, there is a difference in the measured freestream velocity at Mach 1.8. This may originate partly due to temperature variation in the wind tunnel during the run, not captured in CFD. However, as conditions were matched with pressures and Mach numbers, this variation in velocity should have minimal effect on supersonic flow patterns around the bleed holes. Thus, this paper will include only broad quantities from CFD, such as suction mass flow, and instead focus on qualitative flow properties, laying the groundwork for future, correlation level quantitiave comparisons.

Table 3. Differences between CFD and experimental data

Property	Mach 1.8 CFD	% Difference	Mach 2.5 CFD	% Difference
δ (mm)	6.2	6.8%	6.8	9.6%
U_o (m/s)	491	3.4%	575	0.5%
P_e (kPa)	41.7	0.17%	17.9	0.5%
P_o (kPa)	239.9	0.17%	310.2	0.5%

American Institute of Aeronautics and Astronautics

IV. Results and Discussion

A. Flow Visualizations

While characterizing the experimental suction flow rates, schlieren images were taken of the flow over the bleed region, as shown in figure 6, a far-field schlieren image of the experimental setup. Key aspects of the flow which are visible are the expansion fans and barrier shocks generated by each row of bleed holes. The expansion fan is conceptually quite easy to understand, being generated as the flow is turned towards the bleed hole. The barrier shock, so named by previous researchers, is generated primarily by excess flow turned towards the bleed hole by the expansion fan being returned to flow parallel to the floor. In addition, this feature may be associated with slight upflow within the bleed hole itself, and flow spillage. Consecutive expansion fans and barrier shocks are quite easily seen both in the freestream and within the boundary layer.

Figure 6 shows how the expansion fan and shock waves start to interact as they move out from the boundary layer. The leading expansion fan weakens the first barrier shock, which fades into the second expansion fan and so on; the result is that the local pressure gradients abate, and at large distances the wave pattern merges into a single leading expansion fan followed by a weak shock wave. This wave 'merging' is thus an inviscid effect, but is not fully resolved in CFD of the same region in figure 8, where the reduced grid resolution in the freestream results in smearing of the pressure waves. Detailed comparison will thus be restricted to the near-wall region of high fidelity CFD.

Greater detail of the experimental schlieren images is presented in figure 7. Using a horizontal cutoff, the effect of the wall-normal density gradients are integrated over the span of the wind tunnel, and the boundary layer edge is readily visible. The curvature of these waves appears to change as they move through the boundary layer. This feature can be also observed in the CFD results shown in figure 8, although the curvature is not so pronounced as highlighted in experiments - this is primarily due to the fact that Schlieren image integrates the effect of density gradients across the entire working section, while CFD shows the exact density gradient in a single plane. From the comparison between the flow features in the Mach 1.8 and Mach 2.5 cases, it is evident that the angle of the waves is a function of the freestream condition: higher Mach numbers produce a more oblique pattern and vice versa. Moreover at higher plenum pressures, the barrier shock pattern is still present. From CFD it is also evident that the shock structure generated by each successive hole changes, becoming smaller and more oblique.
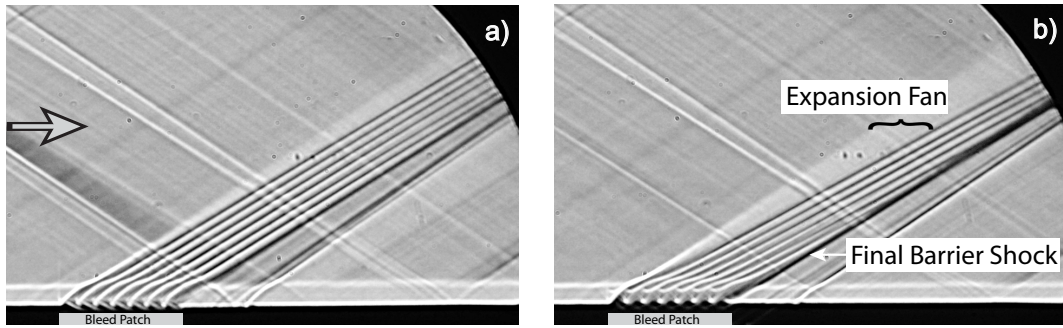
American Institute of Aeronautics and Astronautics

Figure 6. Comparison of far-field schlieren images of Mach 1.8 flow with a) $P_r = 0.89$ b) $P_r = 0.33$.

(a) Mach 1.8 $P_r = 0.89$

(b) Mach 1.8 $P_r = 0.33$
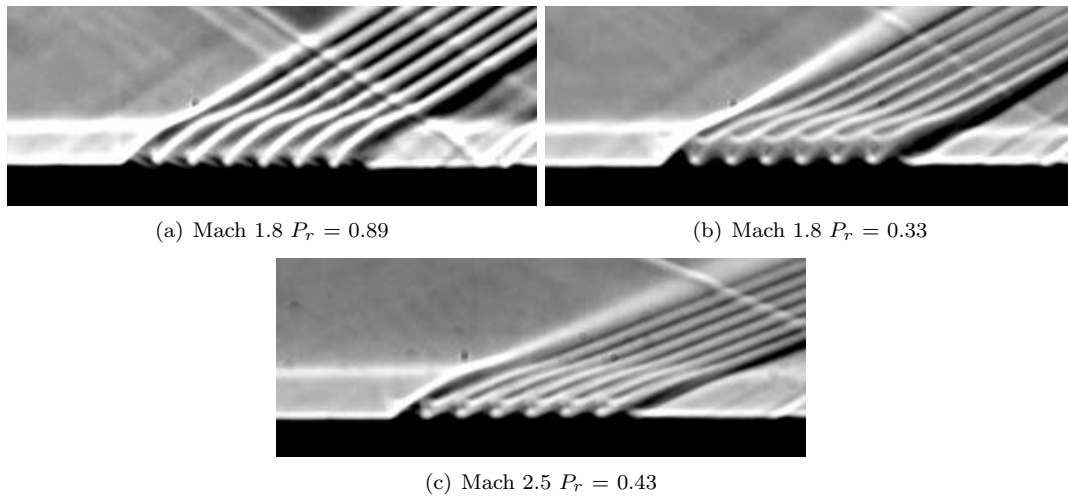
(c) Mach 2.5 $P_r = 0.43$

Figure 7. Experimental schlieren images for M=1.8 and 2.5 flow at $\dot{m}_6$ and $\dot{m}_8$. Flow left to right.
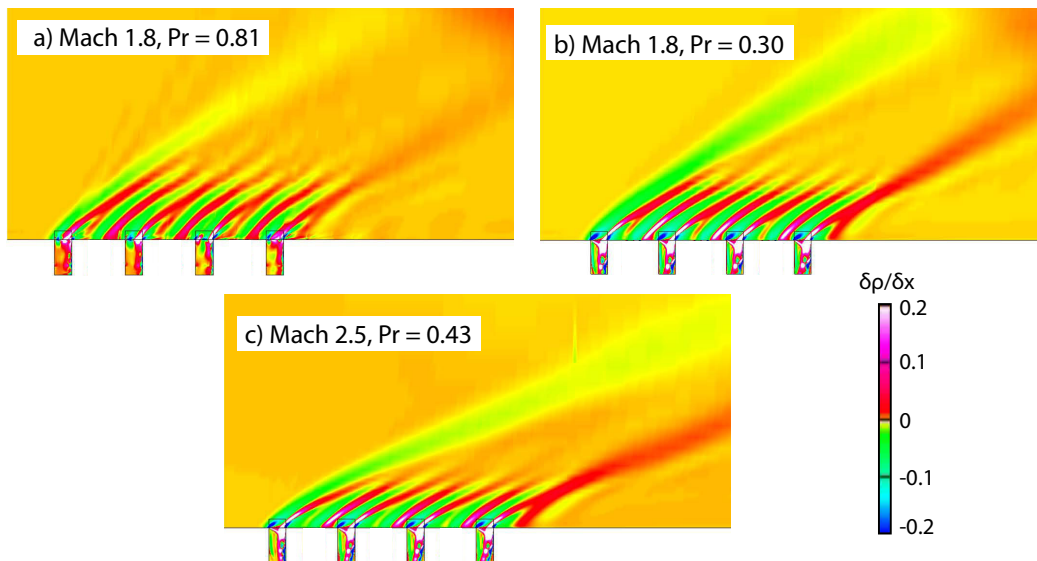

Figure 8. CFD generated density gradients of flow over bleed patch at a) Mach 1.8, $P_r = 0.81$ b) Mach 1.8, $P_r = 0.30$ c) Mach 2.5, $P_r = 0.43$.

B.   Three-Dimensional Flow Structure Investigation

In order to investigate the three-dimensionality of the flow, the LDV measurement volume was traversed across the bleed region with streamwise resolution of 0.5mm to generate contour maps in the $xz-$ and $xy-$planes directly over the bleed region, plus an additional $zy-$plane 8mm downstream of the final row of bleed holes. These various planes are illustrated in figure 9. For the images displaying experimental data, the indicated hole positions are guides only - as mentioned in the methods section, absolute position of the LDV system may be misaligned by 0.2mm, or 10% of a hole diameter. As the relative positioning between data points is reliable to 0.02mm, it is expected that the contour plots show accurate images, simply their placement in the tunnel may be not known as accurately as desired.
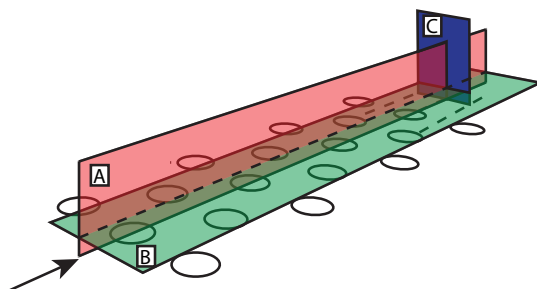

Figure 9.   Illustration of contour plot planes relative to the bleed region.

For the traverses in the $xy-$plane ('A' in figure 9), figures 10 and 11 show data aligned in a vertical plane one hole diameter off centerline, such that the first hole passed over is in the first row (a traverse on the centerline would not clearly show the effects of the first row). Experimental streamlines rely on the fact that this data is taken along a plane of symmetry, thus only streamwise (U) and wall-normal (V) velocity components are required to estimate streamlines.
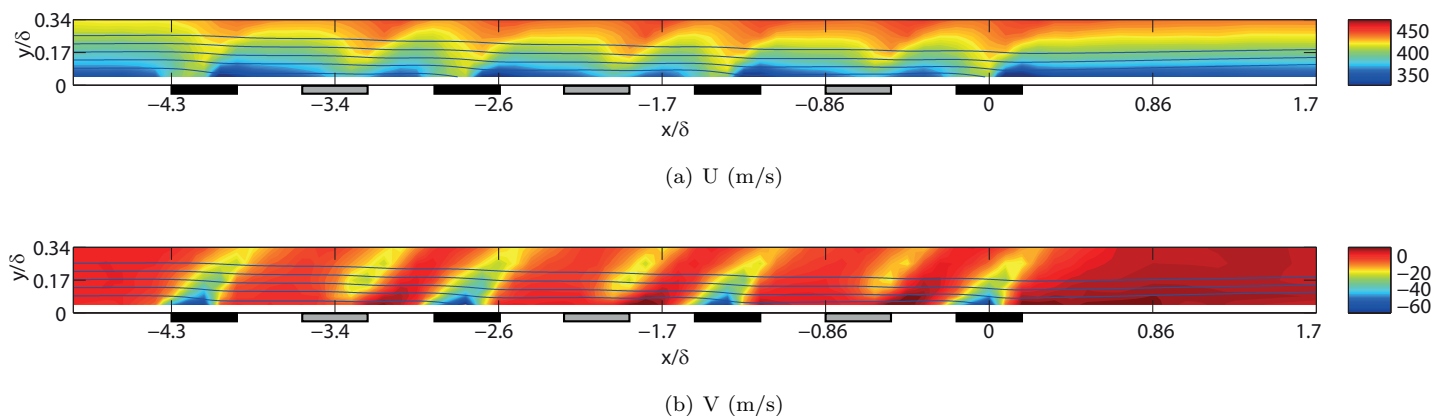

(a) U (m/s)

(b) V (m/s)

Figure 10.   EXP - Mach 1.8 data in a vertical strip directly above a column of holes, at $P_r = 0.32$. Overlaid streamlines derived from U and V data. Grey lines indicate out-of-plane holes.

American Institute of Aeronautics and Astronautics
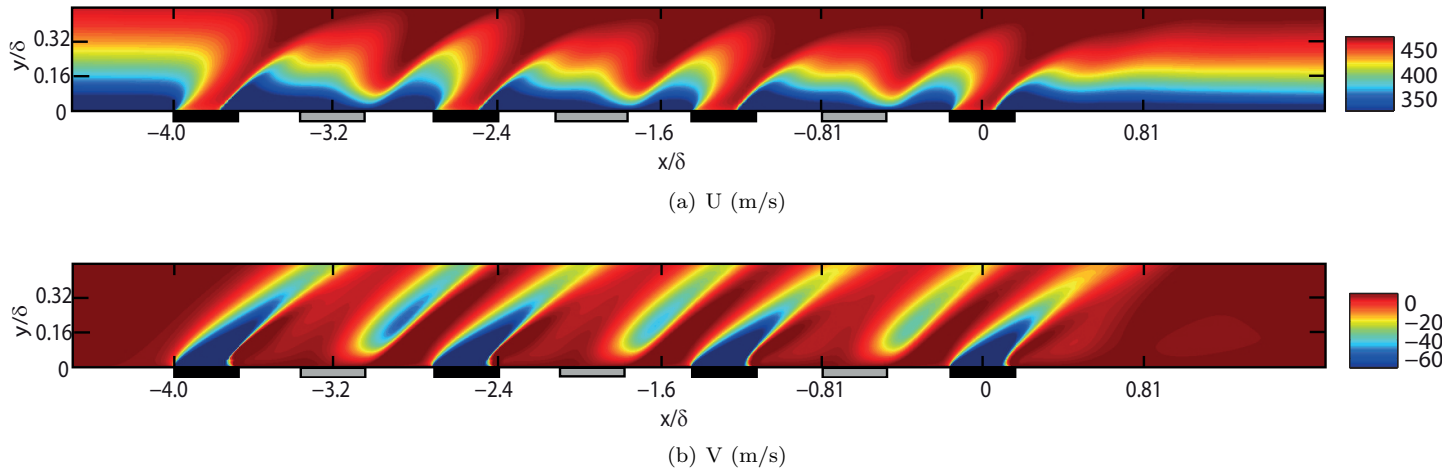
(a) U (m/s)

(b) V (m/s)

Figure 11. CFD generated contour plot of velocities in vertical planes directly above a column of holes, at Mach 1.8, $P_r = 0.30$. Grey lines indicate out-of-plane holes.

The plots of streamwise velocity U show the rapid thinning of the boundary layer over each hole, and a rapid regrowth immediately downstream of each opening before the effects of the next hole are felt. The plots of wall normal velocity V in figure 10(b) clearly show the shock pattern over the bleed region. Faintly visible is the change in curvature of the expansion fan as it passes through the Mach number gradient of the boundary layer. The region of maximum downward velocity, located between the expansion fan and barrier shock in figure 10(b), reduces in size with each successive row of holes. This effect, seen also in the CFD results of figure 11, is due to the higher streamwise velocity and the consequent reduced deflection after each successive hole, and thus a weaker expansion fan.

Differences in the flow can be seen between the Mach 1.8 CFD case, and the Mach 2.5 results in figure 12. Of key interest is the location of the suction peak, the location of maximum measured downward flow (darkest blue region of figures). This region moves towards the downstream edge of the bleed hole as the Mach number is increased. This corresponds with a stronger barrier shock. The CFD data also shows a small region of outflow close to the aft edge of each hole and this positive V-velocity is maintained at least 2 hole-diameters away from the bleed plate. The extent of this thin strip of upwards flow is gradually reduced in the downstream holes; this results from the higher U-velocity near the surface caused by the upstream suction, creating a stronger barrier shock wave with reduced stand-off distance.

CFD allows the visualization of streamlines everywhere inside the fluid domain, which provides interesting and informative results. Figure 13 shows how the streamlines are deflected downward as the flow passes through the expansion fan, and are deflected upwards when the flow is compressed by the barrier shock. This direction change is stronger close to the floor and becomes gradually weaker moving toward the freestream. Generally the streamlines move closer to the floor, and supply the lower boundary layer with higher energy flow. Looking at the plotted streamlines, one can grossly estimate that the flow below $y/\delta = 0.19$ is removed

American Institute of Aeronautics and Astronautics
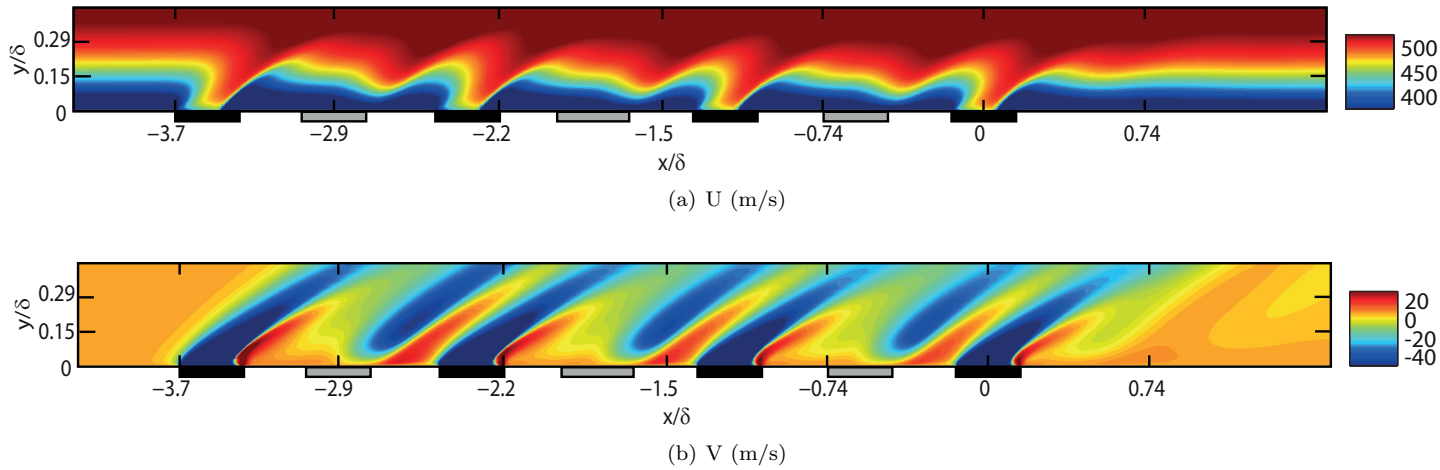
(a) U (m/s)

(b) V (m/s)

Figure 12. CFD generated contour plot of velocities in vertical planes directly above a column of holes, at Mach 2.5, $P_r = 0.43$. Grey lines indicate out-of-plane holes.

from the main flow for this particular setup. This is in rough agreement with the results of experimentally generated streamlines shown in figure 10, which show that almost all of the flow below $y/\delta = 0.17$ is removed by the end of the bleed patch.

Observation of the effect of out-of-plane holes in figures 10 and 11 shows that the bleed hole effect propagates quite strongly in the spanwise direction. Both the barrier shock and expansion fan are found downstream of their generating holes. The streamwise velocity in the layers closer to the floor is also increased after the bleed plate.

To visualize this out-of-plane effect, figure 14 shows a top down view of the bleed array. All streamlines are seeded at the same distance from the wall, but one must recall from figure 13 that the streamlines are drawn closer to the floor as they move towards the right side of the figure. The streamlines are deflected in the z-direction when they pass over a row, except for those ones that are perfectly on the centerline of the holes.

Density gradient isosurfaces of $\partial \rho / \partial x$, evaluated with CFD tools, identify the shape of the expansion fan and barrier shock and are shown in figure 15 around a single hole. It's clearly visible that the outline of the expansion fan is a curved surface that follows the hole edge on the sides. Conversely, the barrier shock waves have a flat front detached from the aft edge of the hole and they are rapidly deflected up from the hole. The curvature of these structures flattens with distance from the floor, due to the different wave angles of expansion fans and barrier shocks; each wave then merges with adjacent waves (in the spanwise direction), thus the structure appears as a single barrier shock in the freestream.

Figure 16 shows a contour plot of properties in the plane at $y/\delta = 0.086$, taken at Mach 1.8, covering a region wide enough to show a full repetition of the bleed hole pattern. The experimental contour map has a streamwise resolution of 0.25 hole diameters, and spanwise resolution of 0.125 hole diameters. One can see the
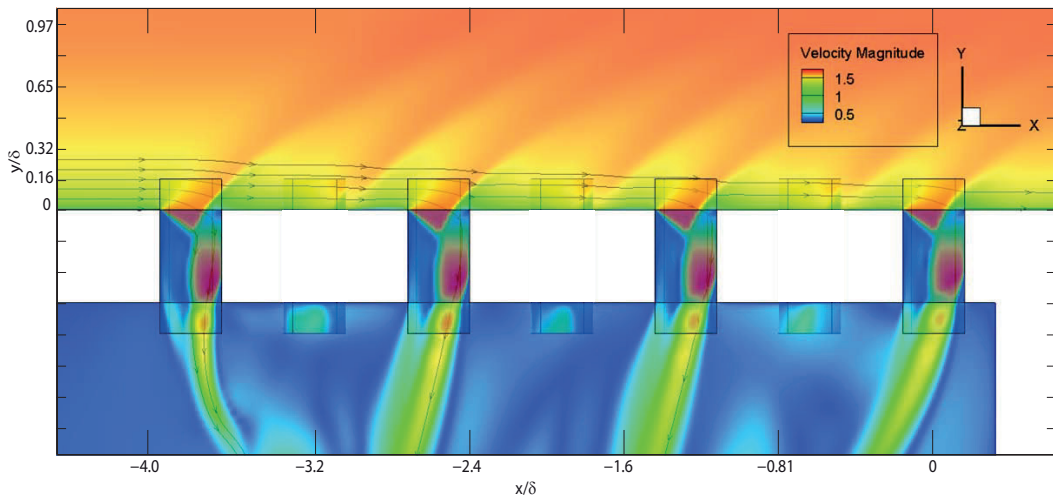
American Institute of Aeronautics and Astronautics

Figure 13. CFD generated streamtraces starting from $y/\delta = 0.002$, 0.05, 0.10, 0.15, 0.19 and 0.24 above the floor, at Mach 1.8, $P_r = 0.30$.
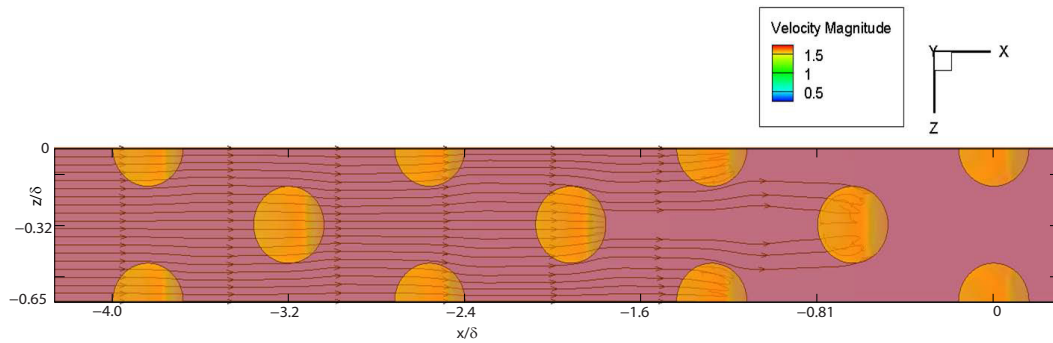

Figure 14. Top-down view of equally spaced streamtraces originating at $y/\delta = 0.19$ above the floor, at Mach 1.8, $P_r = 0.30$.

leading edge of the expansion fans curving around the bleed holes, and joining in the middle. Across the entire bleed region, the streamwise velocity at this height is increased relatively uniformly, by approximately 10% of the freestream velocity, with a spanwise variation of ±3% of the local streamwise velocity. These variations in velocity are not random, but occur in distinct bands aligned with each column of holes, and persist much farther downstream in the experiments than in the CFD. In both the experimental and computational contours, the maximum U velocity over each hole increases with each successive row (darker red in the figure), while the suction peak visible in the wall-normal velocity contour weakens (becomes lighter orange).

The velocities within the various expansion fans and compression areas are visibly similar between the CFD and experimenal data. In these figures, the data from the CFD is much more clear, due in part to its greater spatial resolution. The features appear to extend over a larger area with more distinct boundaries. The difference may stem from two causes; first, that the coarser experimental measurement grid may under-resolve local minima and maxima, and second that there is a non-negligible effect of the LDV measurement
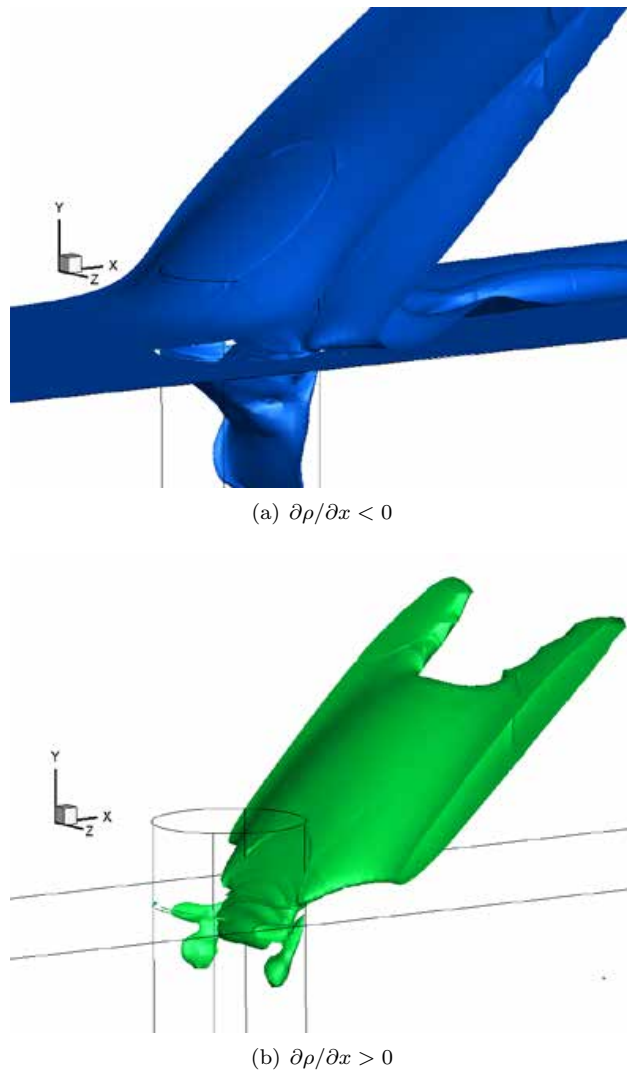
American Institute of Aeronautics and Astronautics

(a) $\partial\rho/\partial x < 0$

(b) $\partial\rho/\partial x > 0$

Figure 15. CFD generated density gradient isosurfaces of $\partial\rho/\partial x$ around a single bleed hole at Mach 1.8, $P_r = 0.30$.

volume. This can smear data across a ± 0.5mm spanwise band on either side of the measurement volume center.

The outflow from the aft edge of the holes can be explained by taking advantage of the numerical streamtraces. Figure 17 displays a close up of a hole and shows the streamtraces hitting the downstream edge. The main flow is deflected downward and accelerated by the expansion fan, and then rapidly decelerated below Mach 1 by the barrier shock. The compression wave also stands off from the edge of the hole, due to the large turning angle required by the flow past the shock. A stagnation point is located just inside the hole on the symmetry line, creating a local high-pressure region. The subsonic flow is deflected by this high pressure, and those particles hitting the edge can travel either upward into the tunnel or downward into the hole. As a result, part of the flow initially entering the bleed hole is then ejected out from it.

Figure 18 a-b) shows the distribution of velocity in the vertical plane is similar between the Mach 1.8

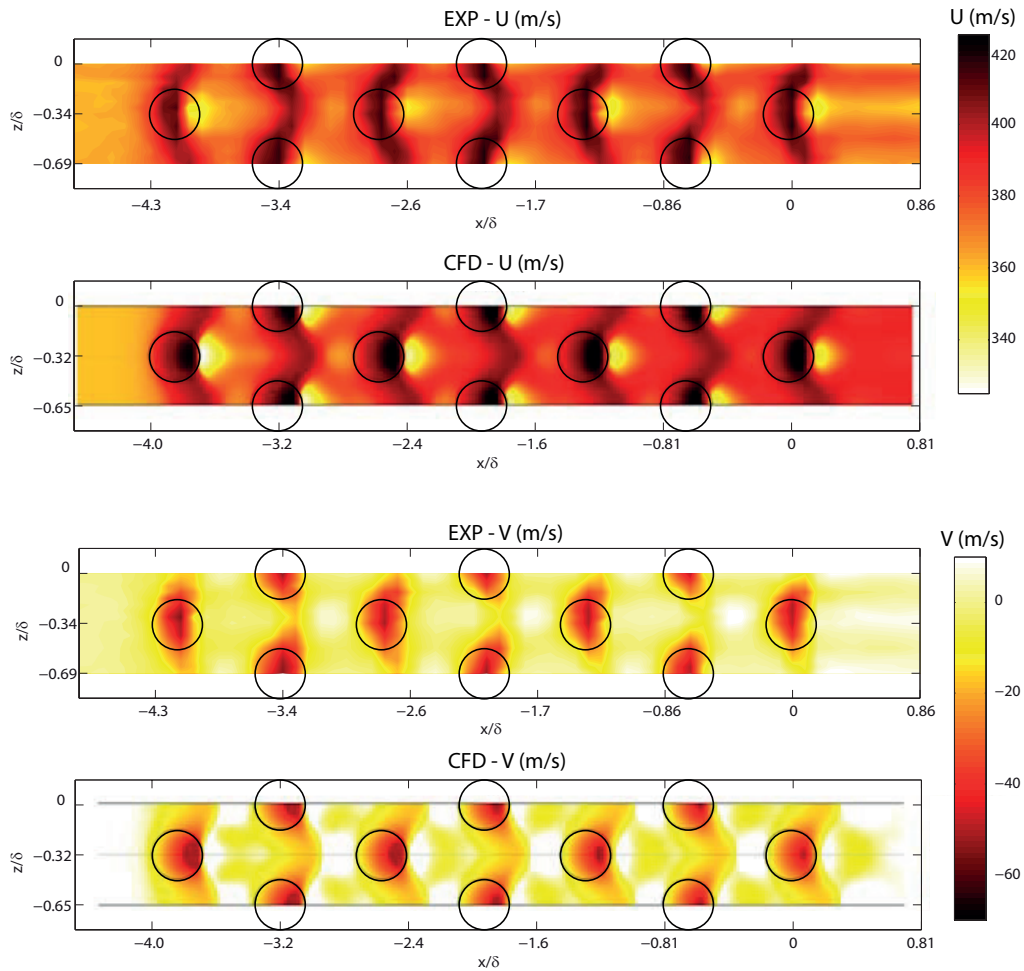American Institute of Aeronautics and Astronautics

Figure 16. Experimental and CFD data used to generate contour plots of U and V at $y/\delta = 0.086$ above the bleed array for experiments, and 0.081 for CFD. Mach 1.8, $P_r = 0.32$ and 0.30 respectively.

and 2.5 cases, but there is a visible difference in the outflow area close to the rear edge of the hole. For the Mach 2.5 case this portion is wider than for the lower freestream speeds case; additionally for the Mach 2.5 case the downward velocity reaches 75 m/s while for Mach 1.8 the top speed is 60 m/s. This is due to the higher static pressure on the edge caused by a stronger deceleration of the main flow impinging the border.

Figure 18 a-b) also shows some interesting aspects of the flow inside the holes, and compares the V-velocity contour map between Mach 1.8 and Mach 2.5 cases. In general, bulk downward flow is confined to the rear half of each hole. In the front half of the hole the V-Velocity is mostly upward, except for a thin layer of downflow near the upstream wall (green in 18 a)). The flow entering the hole is first decelerated by portion of the barrier shock within the bleed hole, and then is re-accelerated above Mach 1, thus supersonic flow enters the plenum. Recirculation regions are present both on the working section and plenum side of the bleed hole. On the plenum side, air is sucked from the plenum into the holes, and re-expelled in the
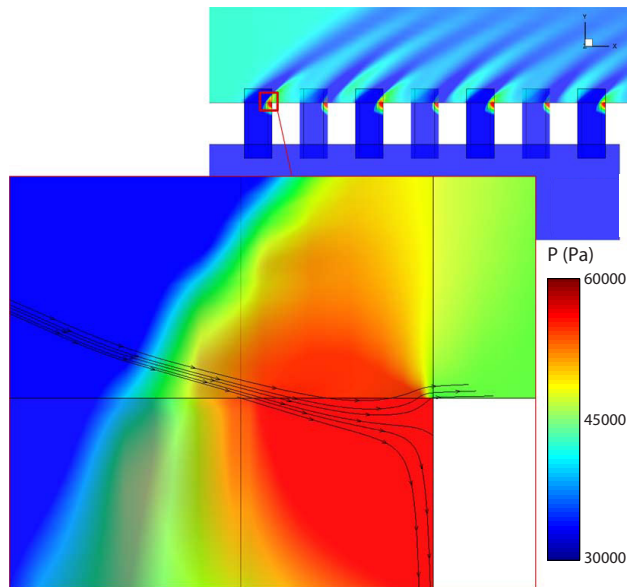
American Institute of Aeronautics and Astronautics

Figure 17. Stagnation point on aft edge of hole. Mach 1.8, $P_r = 0.30$

main downward stream (in blue in figure 18). This occurs on both the upstream and downstream edge of the opening, generating vortices in those interface areas between opposite velocities. Furthermore, in the plane level with the working section floor shown in 18 c-d), it is clear that there is some vertical velocity along the rear edge of the bleed hole, which becomes stronger with increasing Mach number. This jet of strong upwash can contribute to the formation of vortices off the rear of the bleed hole, especially when combined with the downflow to either side of the hole centerline.
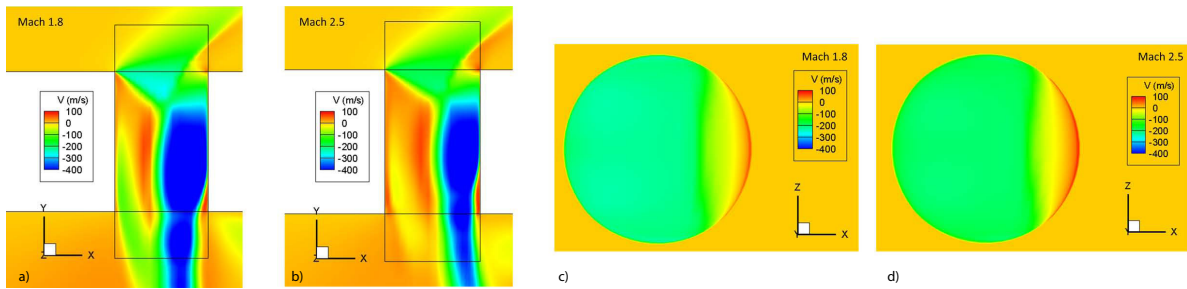

Figure 18. V within a single bleed hole at Mach 1.8 (a,c) and 2.5 (b,d)

Building further on the observation of streamwise bands of higher and lower velocity in figure 16, figure 19 takes additional data from a series of boundary layer traverses. These were performed at Mach 1.8, in a plane normal to the streamwise flow $x/\delta = 1.38$, or 4 hole diameters, downstream of the last row of bleed holes. In these figures, the difference between baseline and suctioned cases are presented as $\Delta U/U_{o\ baseline}$ and ΔV to better highlight differences due to the bleed region. Contour maps of these measurements at maximum suction ($P_r = 0.30$), in figure 19(a), show that in this plane there exists a large spanwise variation in velocity, with a region of strong upflow centered on the hole position, which is also associated with reduced

American Institute of Aeronautics and Astronautics

streamwise velocity when compared to that near the hole edges. Additionally, the effects of the expansion fans and barrier shocks are still distinct and strong, above $y = \delta$.

The same plot is reproduced by CFD in figure 19(b) for $P_r = 0.30$. A similar magnitude of $\Delta U/U_{ob}$ is found near the floor, but the spanwise variation is not as distinct. The velocity along the centerline of the hole is much higher than that seen with experiments, while there is also no upwash directly between two holes. The distinct banding of the expansion fans and barrier shocks is not visible due to the local grid resolution, although the peak downflow is similar to the experiments. Thus, the propagation of the barrier shocks into the freestream is under-resolved, while it appears that the vorticity generated by the bleed holes persists much farther downstream in the experiments than in the computations.

While there is insufficient experimental evidence to directly prove the presence of streamwise voriticity, due to the lack of a third component of measured velocity, there is assembled a set of evidence which may allow one to infer its presence. The combination of flow turning around the edges of the bleed holes and the jet of upwards velocity at the downstream lip of the bleed hole provides a convincing mechanism for vorticity generation. The presence of such an embedded vortex would meanwhile lead to a re-organization of streamwise velocity in the boundary layer, as higher momentum fluid is drawn closer to the floor. Thus, to infer the presence streamwise voriticty, one would generally look to observe variations in streamwise velocity. This is noted twice in the presented data. First, in figure 19(b) where streaks of higher velocity (orange-red) flow persist over 2 hole diameters downstream of the bleed region, in a pattern consistent with upflow along the hole centerline. The second occurance is in figure 19, where the same pattern is seen, and the inferred voriticty pattern drawn.

V.   Conclusions

Overall, there is good agreement between the CFD study, and the associated experimental results. This agreement can be broken into two aspects. First, within the boundary layer the pattern of expansion fans and barrier shocks are almost identical, and react similarly to changes in Mach number and suction strength. Second, velocity maximums and minimums agree to within 10m/s, while suction rates agree to within 3.5g/s, the level of experimental uncertainty. The important aspects of expansion fan and barrier shock patterns are well captured by the CFD within the boundary layer, and are verified by the experiments. The reduced grid resolution in the freestream prevents CFD from resolving the true extent of the pressure waves, which holds implications for modeling more complicated setups and suggests the need for further grid refinement. The improved knowledge of expansion fan and barrier shock dynamics shows that these pressure waves begin to merge as they move away from the bleed hole, while near the floor the effect of a bleed hole has a wider spanwise extent than the hole diameter.

American Institute of Aeronautics and Astronautics

Additionally, streamwise vortices were inferred to develop downstream of the bleed region, caused by the barrier shock interaction, with upwash along the hole centerline agreeing with experimental profiles taken in a plane downstream of the final row of bleed holes. The bulk effects which may be due to vorticity were not seen clearly in CFD, showing a region of further improvement. The detailed flow visualization provided by CFD supports the idea that the high pressure generated by the barrier shock contributes strongly to the development of vorticity.

Future work should focus on attempting to use this knowledge to improve bleed efficiency and control distortion to the flow, while attempting to experimentally study trends linking vorticity with Mach number. Higher resolution studies with LDV should incorporate techniques to reduce the effective measurement volume size, to further improve the data quality in this region.

Acknowledgements

References

[1]Surber, L. and Tinapple, J., "Inlet Flow Control Technology: Learning from History, Reinventing the Future," *50th AIAA Aerospace Sciences Meeting including the New Horizons Forum and Aerospace Exposition*, Aerospace Sciences Meetings, American Institute of Aeronautics and Astronautics, Jan. 2012.

[2]Seddon, J. and Goldsmith, E. L., *Intake Aerodynamics*, 1999.

[3]Harloff, G. J. and Smith, G. E., "On Supersonic-Inlet Boundary-Layer Bleed Flow," *AIAA-95-0038*, 1995.

[4]Hamed, A. and Shang, J. S., "Survey of validation data base for shockwave boundary-layer interactions in supersonic inlets," *Journal of Propulsion and Power*, Vol. 7, No. 4, July 1991, pp. 617–625.

[5]Paynter, G., Treiber, D., and Kneeling, W., "Modeling supersonic inlet boundary layer bleed roughness," *30th Aerospace Sciences Meeting and Exhibit*, Aerospace Sciences Meetings, American Institute of Aeronautics and Astronautics, Jan. 1992.

[6]Slater, J. and Saunders, J., "Modeling of Fixed-Exit Porous Bleed Systems," *46th AIAA Aerospace Sciences Meeting and Exhibit*, Aerospace Sciences Meetings, American Institute of Aeronautics and Astronautics, Jan. 2008.

[7]Slater, J., "Improvements in Modeling 90 Bleed Holes for Supersonic Inlets," AIAA 20090-0710, June, 2009.

[8]Benson, D., Shih, T., Davis, D., and Willis, B., "Boundary conditions for CFD simulations of supersonic boundary-layer flow through discrete holes," *38th Aerospace Sciences Meeting and Exhibit*, Aerospace Sciences Meetings, American Institute of Aeronautics and Astronautics, Jan. 2000.

[9]Chyu, W. J., Rimlinger, M. J., and Shih, T. I.-P., "Control of Shock-Wave/Boundary-Layer Interactions by Bleed," *AIAA Journal*, Vol. 33, No. 7, 1995, pp. 1239–1247.

[10]Shih, T., Benson, T., Willis, B., Rimlinger, M., and Chyu, W., "Structure of shock-wave/boundary-layer interactions with

bleed through rows of circular holes," *35th Aerospace Sciences Meeting and Exhibit*, Aerospace Sciences Meetings, American Institute of Aeronautics and Astronautics, Jan. 1997.

[11]Li, Z., Hamed, A., Manavasi, S., and Nelson, C., "Flow Characteristics through Porous Bleed in Supersonic Turbulent Boundary Layers," *47th AIAA Aerospace Sciences Meeting including The New Horizons Forum and Aerospace Exposition*, Aerospace Sciences Meetings, American Institute of Aeronautics and Astronautics, Jan. 2009.

[12]Hamed, A., Manavasi, S., Shin, D., Morell, A., and Nelson, C., "Bleed Interactions in Supersonic Flow," *International Journal of Flow Control*, Vol. 3, No. 1, March 2011, pp. 37–48.

[13]Orkwis, P. D., Turner, M. G., Apyan, A., Flenar, K., Duncan, S., and Wukie, N., "Modeling and Simulation of Bleed Holes in the Presence of Shock Wave/Boundary Layer Interaction," AIAA 2013-0425, January, 2013.

[14]Hingst, W. R. and Tanji, F. T., "Experimental Investigation of a Two- Dimensional Shock-Turbulent Boundary Layer Interaction with Bleed," AIAA 83-0135, January, 1983.

[15]Willis, B. P., Davis, D. O., and Hingst, W. R., "Flowfield Measurements in a Normal-Hole-Bled Oblique Shock-Wave and Turbulent Boundary-Layer Interaction," AIAA 95-2885, July, 1995.

[16]Willis, B. P. and Davis, D. O., "Boundary layer development downstream of a bleed mass flow removal region," AIAA 96-3278, July, 1996.

[17]Davis, D. O., Vyas, M. A., and Slater, J. W., "Research on Supersonic Inlet Bleed," Vol. 0272, 2012.

[18]Schoenenberger, M., Greber, I., and Davis, D. O., "Flow Measurements Downstream of a Single Bleed Hole in a Subsonic , Turbulent Boundary Layer Using a New 5-Hole Pressure Probe," AIAA 99-0293, January, 1999.

[19]Bodner, J. P., Greber, I., Davis, D. O., and Hingst, W. R., "Experimental investigation of the effect of a single bleed hole on a supersonic turbulent boundary-layer," AIAA 96-2797, July, 1996.

[20]MacManus, D. G. and Eaton, J. a., "Flow physics of discrete boundary layer suction - measurements and predictions," *Journal of Fluid Mechanics*, Vol. 417, Aug. 2000, pp. 47–75.

[21]Oorebeek, J. M. and Babinsky, H., "Flow physics of a normal-hole bled supersonic turbulent boundary layer," *AIAA 2013-0526, 51st Annual Science Meeting, 7-10 January 2013, Grapevine, Texas*, Vol. 0, 2013, pp. 1–23.

[22]Oorebeek, J. M., *Comparison of Distributed Suction and Vortex Generator Flow Control for a Transonic Diffuser*, Ph.D. thesis, University of Cambridge, 2014.

[23]Nolan, W. R., *A Study of Vortex Generator Behavior*, Ph.D. thesis, Cambridge, 2013.

[24]Colliss, S. P., *Vortical structures on three-dimensional shock control bumps*, Ph.D. thesis, Cambridge, 2014.

[25]ISO, "Air distribution and air diffusion - Rules to methods of measuring air flow rate in an air handling duct," *ISO 5221*, 1984.

[26]Bragg, S. L., "Effect of Compressibility on the Discharge Coefficient of Orifices and Convergent Nozzles," *Journal of Mechanical Engineering Science*, Vol. 2, No. 1, 1960, pp. 35–44.

[27]Davis, D. O. and Schoenenberger, M., "Bleed Hole Flow Phenomena Studied," Tech. rep., NASA Lewis Research Center, 1997.
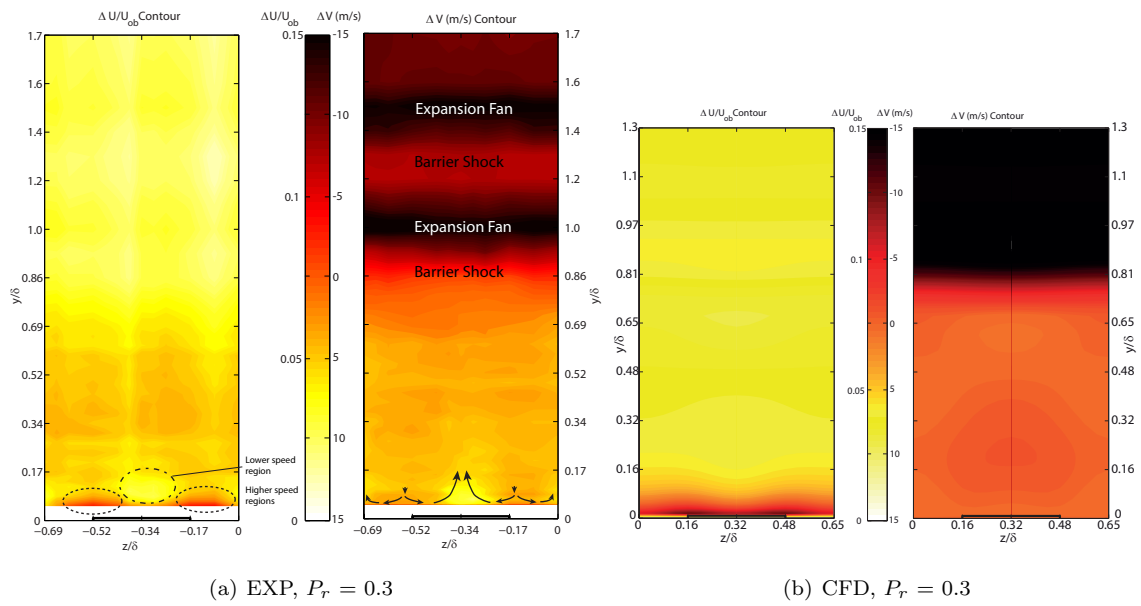
American Institute of Aeronautics and Astronautics

(a) EXP, $P_r = 0.3$ (b) CFD, $P_r = 0.3$

Figure 19. **Change in U and V relative to the baseline boundary layer in the plane** $x/\delta = 1.38$, **or four hole diameters downstream of the last row of bleed holes.**

American Institute of Aeronautics and Astronautics